

ARTICLE

Open Access

Hierarchical highly ordered SnO₂ nanobowl branched ZnO nanowires for ultrasensitive and selective hydrogen sulfide gas sensing

Li-Yuan Zhu¹, Kai-Ping Yuan¹, Jia-He Yang¹, Cheng-Zhou Hang¹, Hong-Ping Ma¹, Xin-Ming Ji¹, Anjana Devi², Hong-Liang Lu¹ and David Wei Zhang¹

Abstract

Highly sensitive and selective hydrogen sulfide (H₂S) sensors based on hierarchical highly ordered SnO₂ nanobowl branched ZnO nanowires (NWs) were synthesized via a sequential process combining hard template processing, atomic-layer deposition, and hydrothermal processing. The hierarchical sensing materials were prepared in situ on microelectromechanical systems, which are expected to achieve high-performance gas sensors with superior sensitivity, long-term stability and repeatability, as well as low power consumption. Specifically, the hierarchical nanobowl SnO₂@ZnO NW sensor displayed a high sensitivity of 6.24, a fast response and recovery speed (i.e., 14 s and 39 s, respectively), and an excellent selectivity when detecting 1 ppm H₂S at 250 °C, whose rate of resistance change (i.e., 5.24) is 2.6 times higher than that of the pristine SnO₂ nanobowl sensor. The improved sensing performance could be attributed to the increased specific surface area, the formation of heterojunctions and homojunctions, as well as the additional reaction between ZnO and H₂S, which were confirmed by electrochemical characterization and band alignment analysis. Moreover, the well-structured hierarchical sensors maintained stable performance after a month, suggesting excellent stability and repeatability. In summary, such well-designed hierarchical highly ordered nanobowl SnO₂@ZnO NW gas sensors demonstrate favorable potential for enhanced sensitive and selective H₂S detection with long-term stability and repeatability.

Introduction

Hydrogen sulfide (H₂S), one of the most dangerous hazardous gases, has aroused widespread concern for its severe toxicity to the human body as well as being normally generated from industries^{1–3}. Trace levels of H₂S are sufficient to damage the human respiratory system as well as cause unconsciousness neurological sequelae and cardiovascular-related death¹. In view of this, it is of great significance to effectively detect and monitor H₂S in the surrounding living environment. To date, diverse

chemical sensors based on different mechanisms have been extensively investigated and developed to detect trace levels of H₂S, including chemiresistive^{4,5}, electrochemical⁶, and optical⁷ sensors. Among these, semi-conducting metal oxide (SMO)-based chemiresistive sensors have attracted tremendous research interest due to their irreplaceable advantages of low cost, convenient fabrication, and great integrated circuit compatibility⁸.

Among various investigated SMOs, tin-oxide (SnO₂) nanomaterials with different morphologies, such as nanoparticles⁹, nanowires (NWs)¹⁰, nanofibers¹¹, and nanobamboos¹², have been intensively explored and regarded as the most promising candidates for high-performance gas sensors, with numerous merits, such as high carrier mobility, great chemical and thermal stability, and low cost^{13,14}. However, these nanostructures are

Correspondence: Hong-Liang Lu (honglianglu@fudan.edu.cn) or David Wei Zhang (dwzhang@fudan.edu.cn)

¹State Key Laboratory of ASIC and System, Shanghai Institute of Intelligent Electronics & Systems, School of Microelectronics, Fudan University, 200433 Shanghai, China

²Inorganic Materials Chemistry, Ruhr-University Bochum, 44780 Bochum, Germany

© The Author(s) 2020



Open Access This article is licensed under a Creative Commons Attribution 4.0 International License, which permits use, sharing, adaptation, distribution and reproduction in any medium or format, as long as you give appropriate credit to the original author(s) and the source, provide a link to the Creative Commons license, and indicate if changes were made. The images or other third party material in this article are included in the article's Creative Commons license, unless indicated otherwise in a credit line to the material. If material is not included in the article's Creative Commons license and your intended use is not permitted by statutory regulation or exceeds the permitted use, you will need to obtain permission directly from the copyright holder. To view a copy of this license, visit <http://creativecommons.org/licenses/by/4.0/>.

usually brush printed or drop coated onto ceramic tubes or microelectromechanical system (MEMS) devices, which intrinsically limits the reliability and repeatability of the fabricated sensors¹⁵. Therefore, a new strategy of seamlessly integrating nanomaterials and microhotplatforms for the sensor fabrication process is of vital importance for obtaining high-performance gas sensors with excellent stability and repeatability, as well as low power consumption. Very recently, a hard template method was developed for in situ monolayer macroporous material synthesis, which fits the requirements mentioned above¹⁶. The in situ preparation process could not only benefit wafer-level fabrication but also effectively reduce the contact resistance and improve the device performance. For instance, Gu et al. prepared an ordered macroporous structure of SnO₂ by employing a monolayer polymethyl methacrylate (PMMA) sphere template, which exhibited excellent repeatability with ethanol and had a promising application in ethanol detection¹⁷. Additionally, such a highly ordered monolayer macroporous structure demonstrated enhanced gas response and response speed due to its large specific surface area and well-interconnected pore structure¹⁸.

However, pristine SnO₂ gas sensors usually suffer from problems such as poor selectivity and long response-recovery time¹⁷. Accordingly, diverse effective approaches have been developed to improve the performance of gas sensors, such as noble metal doping^{19,20}, hierarchical structure construction²¹, and composite heterostructure design^{22,23}. In particular, the construction of hierarchical structures is beneficial for increasing the specific surface area and forming more nanojunctions at the interface between the initial and secondary nanostructures and has been widely regarded as one of the most promising strategies and has stimulated great research interest. For example, Alenezi et al. synthesized hierarchical zinc oxide (ZnO) NWs and nanodisks assembled from initial ZnO nanostructures following a hydrothermal process and demonstrated an enhancement in the acetone sensing performance in comparison to the initial ZnO monomorphological nanostructures²⁴. Furthermore, heterogeneous-hierarchical nanocomposites exhibited superior gas sensing performance than homohierarchical nanostructures considering the synergistic effect of various properties from different materials. Zhang et al. successfully synthesized novel brush-like SnO₂@ZnO hierarchical nanostructures with SnO₂ NW backbones and ZnO nanorod branches via a simple two-step hydrothermal method and demonstrated that the nitrogen dioxide (NO₂) sensing performance of SnO₂@ZnO hierarchical structures was substantially enhanced at a relatively low operating temperature (150 °C) in comparison to that of pristine ZnO and SnO₂²⁵.

Herein, a novel synthetic route for the large-scale fabrication of hierarchical highly ordered SnO₂ nanobowl branched ZnO NWs with excellent H₂S sensing performance is proposed combining a hard template method for the preparation of highly ordered SnO₂ nanobowls, atomic-layer-deposition (ALD) processing of nanoscale ZnO seed layers on the surface of SnO₂ nanobowls, and modified hydrothermal processing for the growth of branched ZnO NWs. In particular, the ALD technique can precisely control the film thickness and provide uniform conformal coverage of ZnO seed layers on SnO₂ nanobowls²⁶. The morphology of the hierarchical structures was tuned by the thickness of the ALD-controlled seed layers and the hydrothermal growth time. The hierarchical branches grown on highly ordered nanobowls can provide an enlarged specific surface area for gas adsorption, as well as efficient channels for electron transport, compared to that of the ZnO film shell²⁷. More importantly, hierarchical sensing materials were synthesized in situ on MEMS devices, which are expected to be high-performance gas sensors with superior sensitivity, long-term stability and repeatability, as well as low power consumption. As a result, the substantially enhanced sensing performance of hierarchical nanobowl SnO₂@ZnO NW gas sensors to H₂S compared to the pristine SnO₂ nanobowl sensor and the heterostructured nanobowl SnO₂@ZnO film sensor was demonstrated. Specifically, the hierarchical nanobowl SnO₂@ZnO NW sensor displayed a high sensitivity (R_a/R_g) of 6.24, a fast response and recovery speed (i.e., 14 s and 39 s, respectively), and an excellent selectivity when detecting 1 ppm H₂S at 250 °C, and its rate of resistance change (i.e., 5.24) is 2.6 times higher than that of the pristine SnO₂ nanobowl sensor. The mechanisms of substantially improved sensing performance were proven by both electrochemical characterization and band alignment analysis, suggesting the synergistic effect of the hierarchical heterostructures, including increased specific surface area, the formation of heterojunctions and homojunctions, as well as the additional reaction between ZnO and H₂S. Moreover, the well-structured hierarchical sensors maintained stable performance after a month, suggesting great stability and repeatability. The combined diversity of hierarchical heterogeneous nanocomposites with low-power MEMS holds favorable potential for highly sensitive and selective H₂S gas sensors with long-term stability and repeatability.

Results and discussion

Figure 1a illustrates the synthetic protocol of the hierarchical highly ordered nanobowl SnO₂@ZnO NWs in situ on MEMS combined with the ALD process. First, highly ordered monolayer polystyrene (PS) spheres soaked with SnCl₄ precursor solution were obtained on

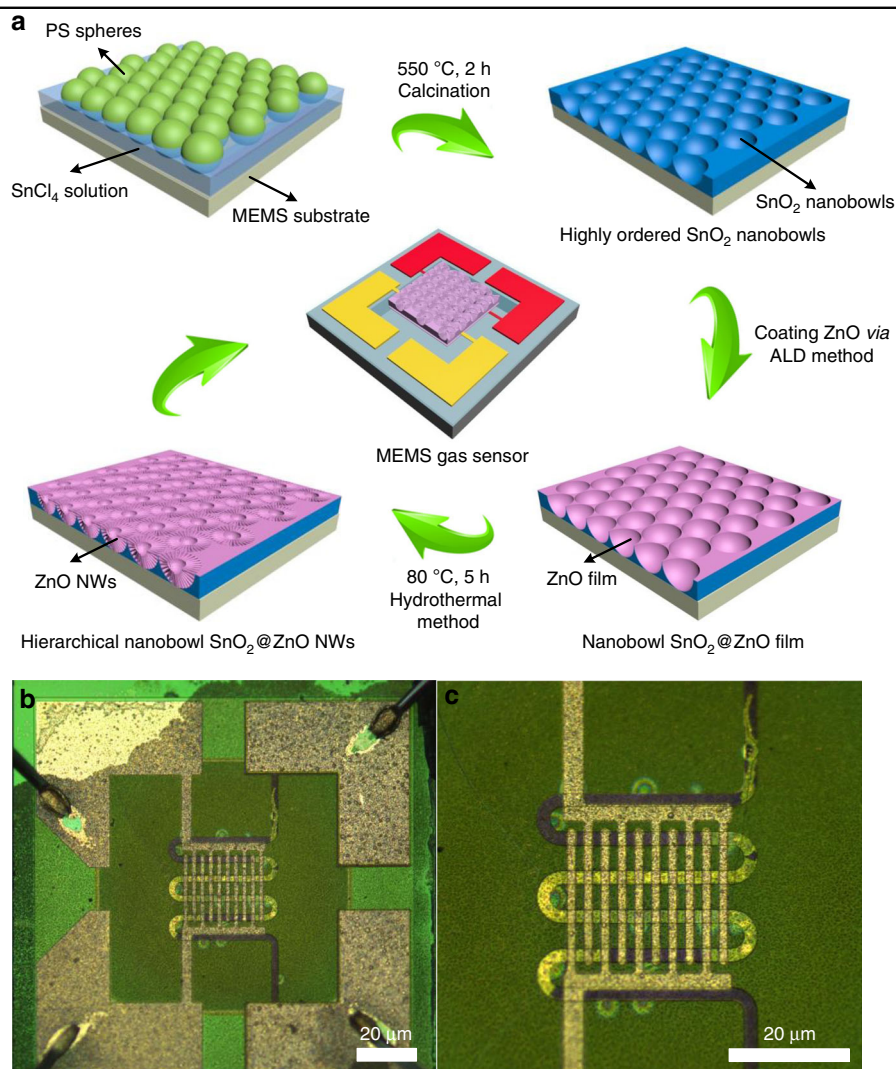
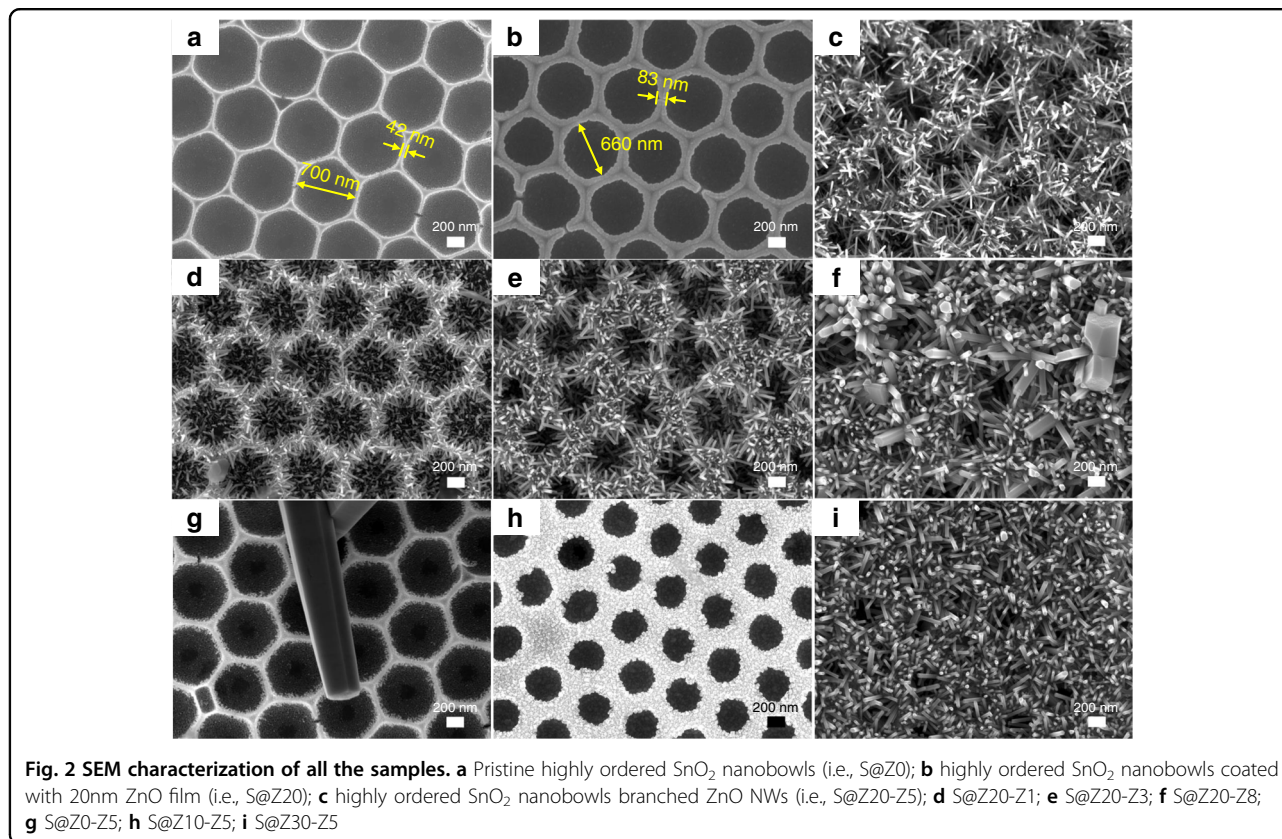


Fig. 1 Synthesis of the hierarchical highly ordered nanobowl $\text{SnO}_2@ZnO$ NWs in situ on MEMS. **a** The synthetic protocol for the hierarchical highly ordered nanobowl $\text{SnO}_2@ZnO$ NWs in situ on MEMS, combining a modified facile hard template method, an ALD process and a hydrothermal method; **b** the optical microscopy image of the MEMS heating appliance with gas sensing materials; **c** an enlarged image of heating electrodes and interdigital sensing electrodes

the MEMS substrate *via* a simple picking-up process. After thorough drying at room temperature and calcination in a muffle furnace at 550 °C for 2 h, the organic PS spheres were removed, and a uniform and shiny highly ordered SnO_2 nanobowl film could be seen on the surface of the MEMS substrate. Figure 1b, c and Fig. S1 show the optical microscopy and SEM images of the MEMS substrate with the obtained materials, displaying the whole structure of the MEMS gas sensor as well as demonstrating the intactness of the device after 550 °C calcination. Figure 2a shows the top-view SEM image of a randomly selected area of the SnO_2 nanobowl film, confirming that the film is composed of highly ordered SnO_2 nanobowls with a diameter of ~ 700 nm. It is noteworthy that the diameter of the nanobowls is slightly shorter than

the diameter of the PS template, which reveals that the SnCl_4 precursor solution level was lower than the half height of the PS sphere. Moreover, since the PS spheres were closely packed on the substrate, an approximate triangular space was naturally formed among three adjacent spheres, exhibiting hexagonal close packing. Then, these highly ordered SnO_2 nanobowls were conformably coated by ZnO seed layers with different thicknesses through thermal ALD at 200 °C. The displayed SEM image in Fig. 2b indicates the as-prepared highly ordered nanobowl $\text{SnO}_2@ZnO$ film morphology with a uniform and conformal ZnO seed layer. The average thickness of the ZnO seed layer turned out to be 20 nm with 100 ALD growth cycles, which is consistent with the result of the ZnO film grown on the flat Si wafer measured by the SE



system. In addition, the thicknesses of the ZnO films with 50 and 150 ALD growth cycles were measured to be 10 and 30 nm, respectively. Evidently, the thickness of the ZnO film shows a continuous increase with a slope of ~ 0.2 nm/cycle when increasing the total ALD growth cycles. The corresponding samples are denoted as S@ZX in this work, where $X = 0, 10, 20,$ and 30 , representing the thicknesses of the ZnO films. Finally, owing to the uniform and conformal coverage of the ZnO seed layer, the ZnO NWs were successfully grown on the surface of the S@Z20 structure via a modified hydrothermal reaction. The ZnO NWs grew densely on the surface of S@Z20, with the highly ordered nanobowl morphology of S@Z20 remaining, appearing similar to a nest-like array (Fig. 2c). The optimal hydrothermal reaction time was further investigated to obtain hierarchical highly ordered nanobowl SnO₂@ZnO NWs with an excellent morphology, which have as large a specific surface area as possible on the basis of maintaining a complete hierarchical structure. Similarly, the corresponding hierarchical samples are denoted as S@Z20-ZY, where $Y = 1, 3, 5,$ and 8 , representing the hydrothermal reaction time.

The morphologies of S@Z20-ZY ($Y = 1, 3, 5,$ and 8) displayed regular changes with an increase in hydrothermal reaction time. At 1 h (Fig. 2d), the branched ZnO NWs were relatively short, and overall, the hierarchical

S@Z20-Z1 retained a macroporous morphology. As shown in Fig. 2d, e and Fig. 2c, when the hydrothermal reaction time is increased from 1 to 5 h (i.e., S@Z20-Z1, S@Z20-Z3, and S@Z20-Z5), the length of branched ZnO NWs is significantly increased, and the whole hierarchical structure seems to be denser. As the hydrothermal reaction time reached 5 h, sample S@Z20-Z5 achieved a maximum length of branched ZnO NWs and maintained a complete hierarchical highly ordered nanobowl branched nanowire structure (Fig. 2c). However, when the hydrothermal reaction time further increased to 8 h, as shown in Fig. 2f, the SnO₂ nanobowls were fully filled with ZnO NWs, which damaged the designed morphology and greatly limited the effective function of SnO₂ nanobowls. In addition, the crystalline grain of ZnO NWs showed a significant increase (Fig. 2f), reducing the specific surface area. As a result, the optimal hydrothermal reaction time for branched ZnO NWs growing on highly ordered SnO₂ nanobowls is 5 h.

Moreover, the effect of the seed layer thickness on the hierarchical nanowire-branched nanobowl structure was further investigated with a determined hydrothermal reaction time of 5 h. Figure 2g-i displays the morphologies of the samples S@Z0-Z5, S@Z10-Z5, and S@Z30-Z5. When the highly ordered SnO₂ nanobowls without a ZnO seed layer were treated with a 5 h hydrothermal process,

branched ZnO NWs could not grow on the surface of the nanobowls, and instead, there would only be nanowires with large grain sizes physically adsorbed on the surface of S@Z0-Z5 across several nanobowls (Fig. 2g). Hence, a uniform and conformal seed layer deposited by ALD is of vital importance to the synthesis of hierarchical structures with branched nanowires. In addition, the thickness of the seed layer would specifically affect the entire hierarchical morphology. It was demonstrated that the highly ordered SnO₂ nanobowls coated with a moderate-thickness ZnO seed layer (i.e., S@Z20-Z5) exhibited the optimal hierarchical structure (Fig. 2c). However, if the seed layer was much thinner (i.e., S@Z10-Z5), there would only be ZnO nanograins on the surface of the seed layer, which were not able to grow into nanowires (Fig. 2h). On the other hand, if the seed layer was too thick (i.e., S@Z30-Z5), the branched ZnO NWs grown *via* the 5 h hydrothermal process would completely fill the nanobowls, thus destroying the designed hierarchical structure (Fig. 2i).

The well-defined hierarchical nanowire-branched nanobowl structure could be further revealed by TEM characterization on a typical sample S@Z20-Z5 (Fig. 3). Figure 3a shows the bright-field TEM image of two single S@Z20-Z5 nanowire-branched nanobowls, clearly displaying the grafting of ZnO NWs on the surface of SnO₂ nanobowls, which is consistent with the SEM results. A highly magnified TEM image (Fig. 3b) indicates the complete morphology and smooth surface of a randomly selected single ZnO NW with a diameter of ~25 nm. The high-resolution TEM (HRTEM) image (Fig. 3c) and the selected-area electron diffraction (SAED) pattern (Fig. 3d) of the randomly selected single ZnO NW on sample S@Z20-Z5 reveal that the branched ZnO nanowires have a single-crystalline structure. The lattice fringes of 0.248 nm and 0.281 nm in the single ZnO NW could be clearly identified, which correspond to the *d*-spacing values of the (101) and (100) planes of the hexagonal wurtzite ZnO phase (PDF#36–1451), respectively.

As shown in Fig. 4a, the crystal structures of hierarchical highly ordered SnO₂ nanobowl branched ZnO NWs were investigated by XRD. Regarding pristine SnO₂ nanobowls, after annealing at 550 °C in air, the measured diffraction peaks could be well indexed into a cassiterite SnO₂ phase (PDF#41–1445). Specifically, the S@Z0 sample showed four characteristic diffraction peaks at 26.6°, 33.9°, 37.9°, and 51.8°, which correspond to the (110), (101), (200), and (211) planes of the cassiterite structure of SnO₂, respectively. Compared to the pristine SnO₂ nanobowls, the S@Z20 core-shell nanobowls obtained after the ALD-ZnO reaction displayed a new strong characteristic diffraction peak at 56.6°, which belongs to the zincite ZnO phase (PDF#36–1451). In addition, three weak diffraction peaks belonging to the SnO₂ phase were not detected in the S@Z20 sample,

which may be affected by the coating of the 20-nm ZnO film. Subsequently, ZnO NWs were further grafted onto the surface of S@Z20 via a hydrothermal process (i.e., S@Z20-Z5), and three additional peaks at 31.7°, 34.4°, and 36.2° were detected, further confirming the hexagonal wurtzite structure of ZnO. Moreover, the prominent ZnO (002) peak indicated that the branched ZnO NWs had a preferential growth orientation along the *c*-axis. It should be noted that no other impurity peak was found in the XRD patterns, which confirmed the phase purity of the prepared samples.

Figure 4b-d and Figure S3 display the XPS spectra of pristine highly ordered SnO₂ nanobowls (i.e., S@Z0) and sample S@Z20-Z5. The full spectrum of S@Z0 in Fig. S3a simply shows the peak positions of Sn 3d and O 1s, revealing the exact SnO₂ composition. By contrast, as shown in Fig. S3c, the additional peaks of Zn 2p and Zn LMM in the full spectrum of S@Z20-Z5 confirm the presence of ZnO in such a heterostructured sample. Specifically, the detailed XPS spectrum of Sn 3d in S@Z0 (Fig. 4b) displays two distinct peaks at binding energies of 487.0 and 495.3 eV, corresponding to the Sn 3d_{5/2} and Sn 3d_{3/2} core levels, respectively. For the detailed XPS spectrum of Sn 3d in S@Z20-Z5 (Fig. 4c), the asymmetric peak could be coherently fitted by two nearly Gaussian components, centered at 495.1 and 498.3 eV. The peak located at 487.0 eV could be assigned to the characteristic Sn 3d_{5/2} peak, which is identical to the typical value of SnO₂. However, the other peak at a higher binding energy of 498.3 eV could be attributed to the Auger electron peak of Zn LMM, demonstrating the existence of Zn in the sample²⁸. Moreover, the Zn 2p XPS spectrum (Fig. 4d) of sample S@Z20-Z5 exhibits the characteristic Zn 2p_{3/2} and Zn 2p_{1/2} peaks centered at 1021.3 and 1044.3 eV, respectively, which confirms the presence of ZnO composition. The detailed O 1s spectra of S@Z0 and S@Z20-Z5 can be found in Fig. S3b and d. Both asymmetric O 1s peaks could be deconvoluted into two parts, assigned to oxygen in the SnO₂ or ZnO crystal lattice and the surficial adsorbed oxygen, respectively²⁹.

The prepared samples were all synthesized *in situ* on MEMS structures to form the proposed gas sensors, as shown in Fig. 1. The JF02F gas sensing measurement system was used to evaluate the gas sensing properties of all the sensors. Typically, three representative MEMS-based sensors (i.e., sample S@Z0, S@Z20, and S@Z20-Z5) were chosen as examples for further investigation of gas sensing performance. The S@Z0 sample was only a highly ordered SnO₂ nanobowl monolayer film with neither ZnO seed layers nor a hierarchical branched nanowire structure. The S@Z20 sample had a 20-nm-thick seed layer of ZnO film, and the S@Z20-Z5 sample had further branched ZnO NWs with optimal length and diameter on the basis of a ZnO seed layer. First, the response of a gas sensor is greatly

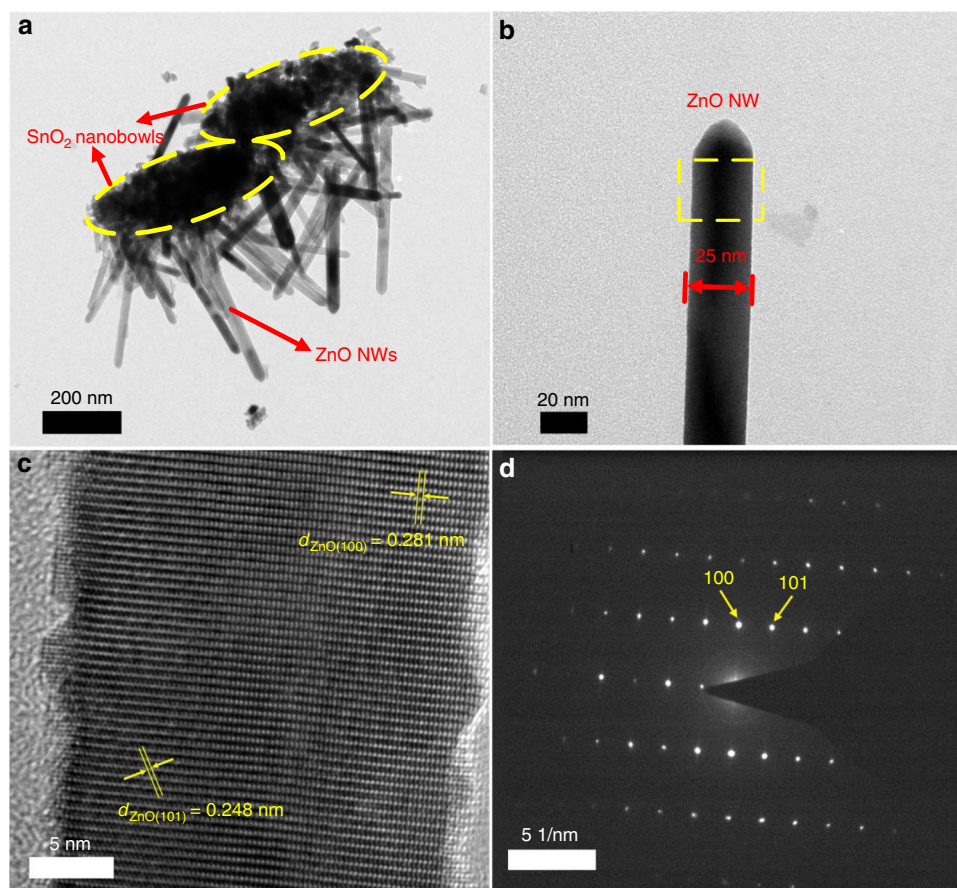
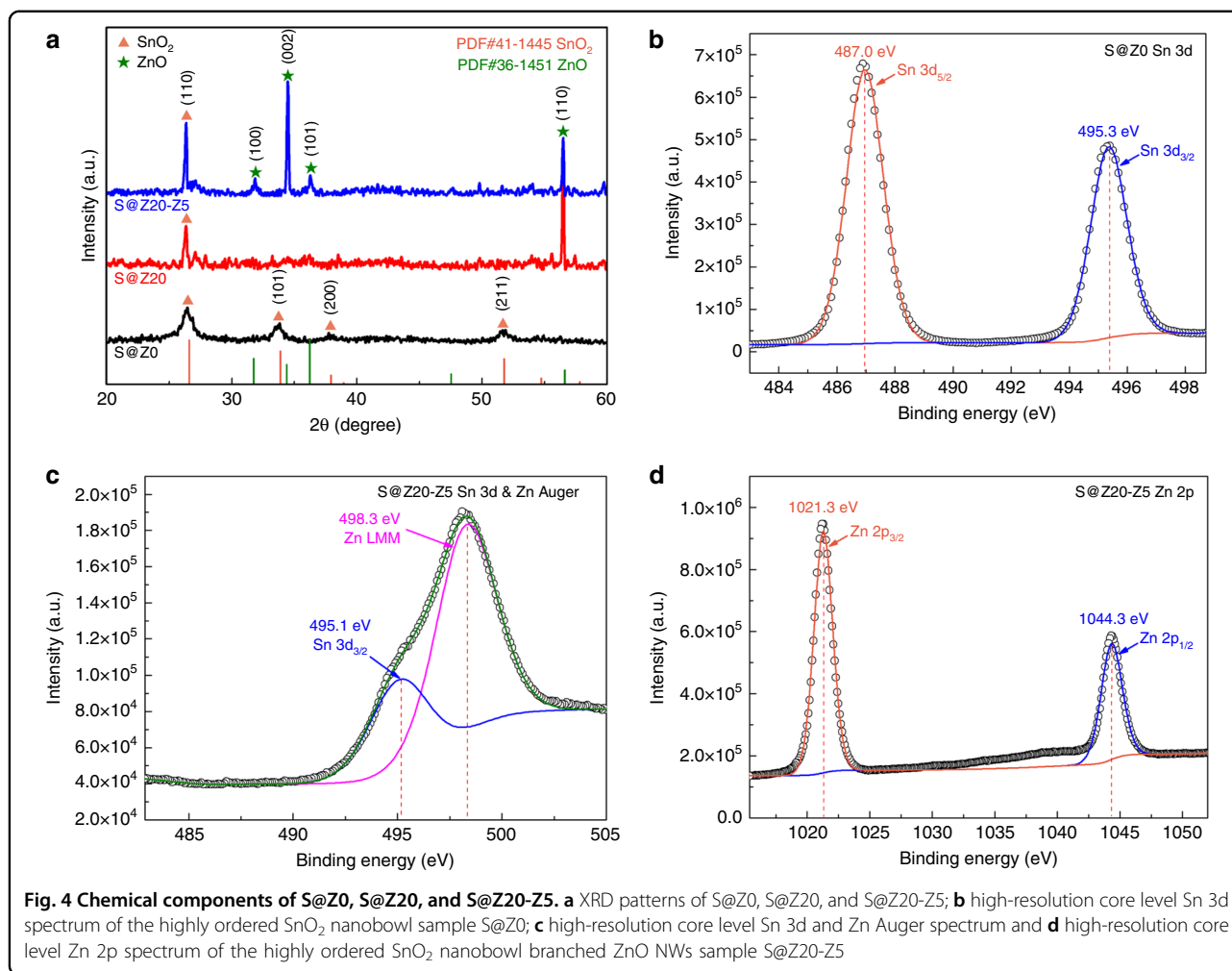


Fig. 3 TEM characterization of the highly ordered SnO₂ nanobowl branched ZnO NW sample S@Z20-Z5. **a** Low-magnification image of two nanowire-branched nanobowls; **b** the highly magnified image of a randomly selected single ZnO NW on S@Z20-Z5; **c** the HRTEM image and **d** the SAED pattern obtained on a single ZnO NW

affected by the operating temperature. Hence, the relationship between the gas sensing response and the operating temperature was first investigated in Fig. 5a. For all the sensors, their gas sensing responses continued to grow as the operating temperature increased from 100 to 250 °C. All the sensors yielded maximum responses at 250 °C, indicating that the optimal operating temperature for the designed materials in this work could be chosen as 250 °C. However, all the responses began to decrease as the operating temperature further increased above 250 °C (i.e., 300 °C). H₂S molecules will have difficulty reacting with adsorbed oxygen at a low operating temperature but will desorb before the reaction can occur at an excessively high operating temperature¹⁸. In addition, the diffusion rate of H₂S molecules adsorbed on the material surface will improve with increasing temperature³⁰. Therefore, at the optimal operating temperature of 250 °C, the gas sensing responses achieved maxima. The S@Z20-Z5 sensor displayed the highest response at any temperature.

Figure 5b shows the corresponding dynamic gas sensing response curves of all the samples (i.e., sample S@Z0,

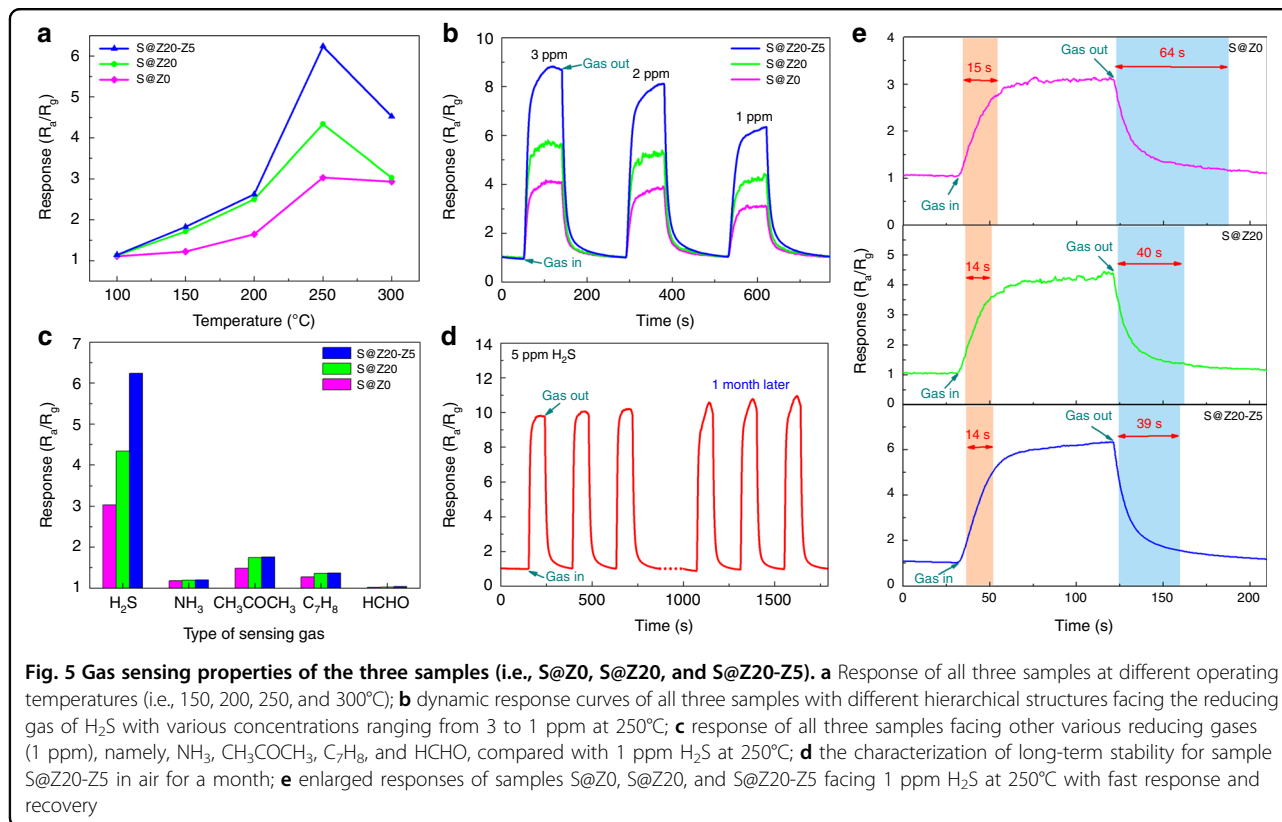
S@Z20, and S@Z20-Z5) with different hierarchical structures at the optimal operating temperature of 250 °C, obtained for the reducing gas of H₂S with various concentrations ranging from 3 to 1 ppm. Apparently, the responses of all samples decrease as the H₂S concentration decreases. More importantly, compared with the pristine highly ordered SnO₂ nanobowl gas sensor (i.e., S@Z0), the designed hierarchical nanobowl SnO₂@ZnO NW gas sensor (i.e., S@Z20-Z5) does exhibit superior gas sensing performance, which may be closely related to both the construction of the heterostructure and the effective increase in the specific surface area. Specifically, when the H₂S concentration was fixed to 1 ppm, the response of S@Z20-Z5 was approximately 6.24, whose rate of resistance change (~5.24) was 2.6- and 1.6-fold those of the S@Z0 (~2.03) and S@Z20 (~3.34) sensors, respectively. Table 1 presents the sensing performance comparison of the prepared S@Z20-Z5 sensor with various other SnO₂-based gas sensors fabricated on MEMS^{31–36}. Comprehensively considering the related factors, including operating temperature, response values



and response/recovery time, the S@Z2O-Z5 sensor shows improved performance among the MEMS-type SnO₂-based gas sensors.

To investigate the time dependence of the response, Fig. 5e shows the transient responses of all three samples exposed to 1 ppm H₂S at 250 °C. The response time and recovery time were measured as the time taken for the sensor output to change from 10 to 90% of the highest response variation. The recovery time of S@Z2O-Z5 is 39 s, which obviously exhibits a better recovery property than the pristine S@ZnO sensor (i.e., 64 s). However, the recovery time of S@Z2O-Z5 (i.e., 14 s) is slightly shorter than that of S@ZnO (i.e., 15 s). This indicates that compared with the pristine S@ZnO sensor, the S@Z2O-Z5 sensor exhibits a faster response when exposed to H₂S gas. At the same time, the S@Z2O-Z5 sensor possesses a better recovery property when turning off the gas and flushing with air. Actually, the existence of the SnO₂@ZnO heterojunction will improve the hole-electron separation rate at the interface, therefore improving the response and recovery speed to some extent³⁷.

In practice, good selectivity is a critical factor for a gas sensor, especially for distinguishing the given target gas from a complex atmosphere. Herein, the selectivity of the S@Z2O-Z5 sensor was studied towards H₂S and various other reducing gases (1 ppm), such as ammonia (NH₃), acetone (CH₃COCH₃), methylbenzene (C₇H₈), and formaldehyde (HCHO), at an operating temperature of 250 °C, which is shown in Fig. 5c and Fig. S4. It can be observed apparently that the responses of all three samples to H₂S are significantly higher than those of other reducing gases, especially for the S@Z2O-Z5 sensor, confirming the excellent selectivity. Generally, the selectivity is related to various complicated factors. First, H₂S has a relatively small band dissociation energy of 381 kJ/mol compared with other gases, which promotes decomposition and surface reactions during chemical adsorption at lower temperature³⁸. As for the accurate calculation of the corresponding surface reaction kinetics, first-principles calculations based on density functional theory could be applied, which needs to be further investigated³⁹. Second, the XPS characterization of the



SnO₂@ZnO heterostructures before and after the H₂S-sensing test conducted by Fu et al. has demonstrated that ZnO will react with H₂S and transfer to ZnS, leading to a larger response since the conductivity of ZnS is higher than that of ZnO⁴⁰. Furthermore, the reaction between ZnO and adsorbed H₂S is an exothermic and spontaneous process, while the reactions between ZnO and other test gases are endothermic and nonspontaneous⁴¹. Therefore, the introduction of branched ZnO NWs further enhances the selectivity to H₂S. Finally, H₂S is considered to possess a larger adsorption capacity on the same surface adsorption area, which is attributed to the relatively small molecular size of H₂S among these gas molecules. In addition, the S@Z20-Z5 sensor has a better selectivity than the one based on pristine SnO₂ nanobowls. This phenomenon further confirmed the important role of the proposed branched ZnO NWs in improving the selectivity.

On the other hand, stability is also a key parameter from the viewpoint of practical gas sensing applications. The assessment of long-term stability was carried out on S@Z20-Z5 in ambient air for a month, as shown in Fig. 5d. Obviously, after a month, the S@Z20-Z5 sensor exhibited less than 5% variation in response when exposed to 5 ppm H₂S, illustrating good long-term stability. However, it is undeniable that the response of the S@Z20-Z5 sensor exhibited a slight increase after a

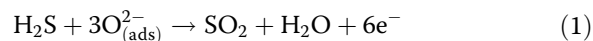
series of H₂S gas sensing measurements for a month. The slightly higher response after a month may be caused by a few ZnS residual on the surface of the sensing material, which was transformed from ZnO in the presence of H₂S and had a higher conductivity than ZnO. Fortunately, since the residual ZnS could be retransformed into ZnO more thoroughly at a higher temperature than the operating temperature of 250 °C⁴², the response after a long-term test can return to the original value with the help of a high-temperature thermal treatment. Moreover, the top-view SEM image of a randomly selected area of S@Z20-Z5 after the above long-term tests is shown in Fig. S5. The intact hierarchical nanowire-branched nanobowl structure further demonstrated good long-term stability.

In general, the gas sensing mechanism is based on the surface adsorption/desorption model of oxygen species⁴³. It was observed in Fig. S6 that the resistances of all three sensors show a sudden decrease when introducing the reducing gas of H₂S, indicating that the sensors exhibit typical *n*-type conductivity behaviors according to the acknowledged mechanism for the SMO-based resistance-type gas sensors⁴⁴. Specifically, when the *n*-type sensor was exposed to air, the physically adsorbed oxygen on the surface would capture electrons from the conduction band of sensing materials and turn into chemisorbed oxygen such as O₂⁻, O₂²⁻, O⁻ or O²⁻^{45,46}. Therefore, an

Table 1 Sensing performance comparison of various SnO₂-based gas sensors fabricated on MEMS

Materials	Target gas	Response (R _a /R ₀)	Operating temperature [°C]	Response time [s]	Recovery time [s]
Porous SnO ₂ 3D architectures ³¹	HCHO (0.5 ppm)	2.9	240	/	/
SnO ₂ -ZnO composite nanofibers ³²	NO ₂ (50 ppm)	3.3	25	264	294
Hierarchical SnO ₂ -ZnO NWs ³³	C ₂ H ₅ OH (25 ppm)	3.0	400	/	/
SnO ₂ /ZnO core-shell nanosheets ³⁴	C ₂ H ₅ OH (100 ppm)	13.3	350	/	/
Hierarchical SnO ₂ -ZnO nanofibers ³⁵	CH ₃ OH (2 ppm)	3.4	250	18	25
Porous SnO ₂ -ZnO hybrid nanotubes ³⁶	H ₂ S (1 ppm)	4.29	220	93	205
Hierarchical nanobowl SnO ₂ @ZnO NWs (this work)	H ₂ S (1 ppm)	6.24	250	14	39

electron-depleted region formed underneath the material surface, causing the sensing material to be in a high-resistance state. Once the *n*-type sensor was exposed to the reducing gas of H₂S, the chemisorbed oxygen species on the surface would react with H₂S and release the electrons back to the material, as typically shown in Eq. (1)³:



Therefore, the resistance of the *n*-type sensor will achieve a rapid decrease when introducing the reducing gas, which is in accordance with the experimental results shown in Fig. S6. The three-dimensional schematic of S@Z20-Z5 exposed to H₂S gas is shown in Fig. 6a.

The experimental results in Fig. 5b observably show that the sensing properties of the highly ordered SnO₂ nanobowl branched ZnO NW sensor (i.e., S@Z20-Z5) were much better than that of the pristine SnO₂ nanobowl sensor (i.e., S@Z0). There are three main factors that satisfactorily account for the enhancement of gas sensing performance. First, due to the introduction of hierarchical branched ZnO NWs, the increase in specific surface area effectively increases the active adsorption sites and enhances the sensing response²⁴. To provide direct experimental evidence for the increase in specific surface area, the electrochemically active surface areas of S@Z20 and S@Z20-Z5 were measured through electrical double-layer capacitance (EDLC) measurements in Na₂SO₄ solution on the basis that the double-layer capacitance (C_{dl}) is proportional to the electrochemically active surface area⁴⁷. The cyclic voltammetry (CVs) were tracked in the range of -0.30 to -0.19 V, where the current response should only refer to the charging of the double layer. The CV curves of the S@Z20 and S@Z20-Z5 electrodes at different scan rates (1, 2.5, 5, 7.5, 10, 15, 20, 25, and 30 mV/s) are shown in Fig. S7a, b, respectively. As a result, the capacitance of the S@Z20-Z5 electrode (0.223 mF/cm², Fig. S7d) is higher than that of the S@Z20 electrode (0.119 mF/cm², Fig. S7c), indicating the higher active surface area of the S@Z20-Z5 electrode, which is consistent with the SEM results. Therefore, on the basis of the CV measurements, the hierarchical heterostructured S@Z20-Z5 sample had a higher specific surface area than S@Z20, which effectively increased the number of gas adsorption sites.

Second, the cause of the resistance modulation could be the formation of the SnO₂@ZnO heterojunction and ZnO@ZnO homojunction at the corresponding interfaces³³. The separate band alignment diagrams of SnO₂ and ZnO are displayed in Fig. 6b. Since the work function of ZnO (5.2 eV) is larger than SnO₂ (4.9 eV), when the ZnO film as well as ZnO NWs were grown onto highly ordered SnO₂ nanobowls, the electrons would be

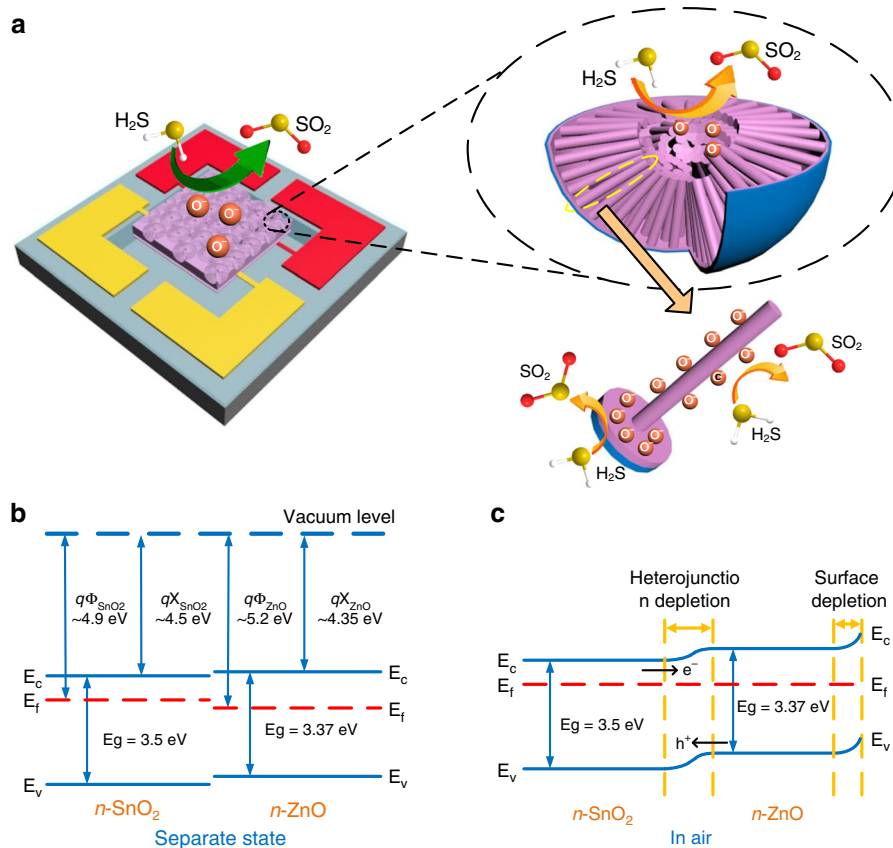


Fig. 6 Schematics of the reducing gas sensing mechanism in the hierarchical highly ordered nanobowl SnO₂@ZnO NWs. **a** The three-dimensional schematic of the hierarchical highly ordered nanobowl SnO₂@ZnO NWs exposed in H₂S gas; **b, c** the schematic energy band diagrams for the hierarchical SnO₂@ZnO NWs: **b** in separate state and **c** in air. The band structure data in figure (b) were determined from the literature⁴⁸

transferred from SnO₂ to ZnO to equalize the Fermi level, leading to the formation of a potential barrier at the *n-n* heterojunction interface (Fig. 6c)⁴⁸. As a result, the resistance of the *n*-type S@Z20-Z5 sensor (R_a) achieved a further increase in air because of the additional existence of a potential barrier formed at the SnO₂@ZnO heterojunction interface. Correspondingly, when the S@Z20-Z5 sensor was exposed to the reducing gas of H₂S, the decrease of the heterojunction barrier could help further reduce the resistance (R_g), leading to the enhancement of the sensing response defined as R_a/R_g . Moreover, 20 nm is close to the Debye length of ZnO (~20 nm) at 250 °C, which further benefits the improvement of gas sensing performance⁴⁰. In addition, the ZnO@ZnO homojunction at the contact area of branched ZnO NWs was also attributed to resistance modulation, increasing the resistance in air and further reducing the resistance in reducing gas.

The third factor is the transformation of ZnO to ZnS during the spontaneous reaction with H₂S^{40,41}. When

ZnO is exposed to H₂S, a small amount of ZnO reacts with the adsorbed H₂S and turns into ZnS on the surface, as shown in Eq. (2):⁴⁹



Since the conductivity of the reaction product ZnS is higher than that of ZnO, the resistance of the whole material would achieve a further decrease after introducing H₂S and undergoing such a transformation reaction⁴⁰. Correspondingly, when the material was exposed to air again, the small amount of ZnS on the surface reacted with adsorbed oxygen and retransformed into ZnO at the high operating temperature⁴². Therefore, the introduction of ZnO film and branched ZnO NWs further improves the sensitivity of the heterostructured SnO₂@ZnO sensors. Meanwhile, as mentioned above, the spontaneous reaction between ZnO and H₂S enhances the selectivity of the heterostructured sensors for H₂S detection as well.

Materials and methods

Chemicals and reagents

Analytical grade tin (IV) chloride hydrate (SnCl_4) was obtained from Alfa Aesar. Zinc nitrate hexahydrate [$\text{Zn}(\text{NO}_3)_2 \cdot 6\text{H}_2\text{O}$] and hexamethylenetetramine ($\text{C}_6\text{H}_{12}\text{N}_4$) were purchased from Aladdin. Sodium dodecyl sulfate (SDS) as the surfactant was obtained from Sinopharm Chemical Reagent Co., Ltd. The precursor materials used for depositing the ZnO layer were diethyl zinc [$(\text{C}_2\text{H}_5)_2\text{Zn}$, DEZ, Sigma Aldrich, 99.999%] and deionized (DI) water. All chemicals were used as received without any further purification. Other chemical reagents employed in our experiments were analytical grade, and the gases were ultrahigh pure (99.999%). All aqueous solutions were prepared with DI water acquired from a Millipore Q purification system (resistivity $>18 \text{ M}\Omega \cdot \text{cm}$).

Synthesis of highly ordered SnO_2 nanobowls

The highly ordered SnO_2 nanobowls were synthesized via a modified hard template method reported before¹⁸. The suspension of monodispersed PS spheres 800 nm (2.5 wt% in DI water) in diameter was synthesized according to our previous work⁵⁰. Then, the PS suspension was diluted in ethanol of the same volume and subjected to ultrasonic treatment for absolute uniformity. The precursor solution was 0.1 M aqueous SnCl_4 (100 mL). The ethanol-diluted PS suspension was slowly injected into the precursor solution, and the monolayer PS spheres could float on the surface of the precursor solution and began to self-assemble at the air/solution interface. Specifically, the control of the injection rate was conducted by adjusting the inclination angle of the well-cleaned and oxygen plasma pretreated glass slide, which was applied as a drainage plate. Subsequently, the floating PS monolayer was transferred to the MEMS substrate by a simple picking-up process and thoroughly dried at room temperature. Due to the capillary effect, the PS monolayer on the substrate still retained the precursor solution in the spaces between PS spheres and the substrate¹⁵. After annealing in the muffle furnace at 550 °C for 2 h, the organic PS template was well removed, and highly ordered SnO_2 nanobowls were formed in situ on the MEMS substrate.

Synthesis of highly ordered nanobowl $\text{SnO}_2@ZnO$ films

ZnO seed layers of different thicknesses, namely, 50, 100, and 150 cycles, were deposited at 200 °C on as-prepared highly ordered SnO_2 nanobowls in a BENEQ TFS-200 ALD system. Briefly, DEZ and DI water were used as the zinc (Zn) and oxidant sources, respectively. The highly ordered SnO_2 nanobowls were alternately exposed to the vapor pulse of the DEZ and DI water precursors in the ALD reactor chamber using high purity argon gas as the carrier gas. Meanwhile, the high purity Ar

as the purge gas purged the gaseous byproducts and residual gas out of the chamber between two valid pulses, effectively avoiding unexpected gas reactions. For all samples, the deposition process in each growth cycle briefly includes a 0.2 s pulse of DEZ, a 10 s purge, a 0.2 s pulse of DI water and a 10 s purge. The different desired thicknesses of ZnO seed layers can be achieved by repeating different specific ALD growth cycles.

Synthesis of hierarchical highly ordered nanobowl $\text{SnO}_2@ZnO$ NWs

ZnO NWs were grown on highly ordered nanobowl $\text{SnO}_2@ZnO$ films with different ZnO seed layers through a traditional hydrothermal process⁵¹. In particular, an aqueous solution containing 25 mM $\text{Zn}(\text{NO}_3)_2 \cdot 6\text{H}_2\text{O}$ and 25 mM $\text{C}_6\text{H}_{12}\text{N}_4$ was prepared as the precursors for ZnO NW growth and transferred into 80 mL Teflon-lined stainless steel autoclaves. Then, highly ordered nanobowl $\text{SnO}_2@ZnO$ films on MEMS substrates were submerged in the solution with face down. The hydrothermal reactions were carried out at 80 °C for different reaction times, namely, 1, 3, 5, and 8 h, and then cooled to room temperature. The substrates were then removed from the solution, rinsed thoroughly with DI water and dried with high pure nitrogen.

Instruments and characterization

A BENEQ TFS-200 ALD system was used to deposit the ZnO seed layers. The thicknesses of the ZnO films deposited on flat silicon substrates were measured by a SOPRA GES-5E spectroscopic ellipsometry (SE) system. The morphologies of all the samples were recorded on a Zeiss SIGAMA HD field-emission SEM and an FEI Tecnai G² F20 S-TWIN field-emission TEM. Wide-angle XRD patterns were collected on a Bruker D8 Advance powder X-ray diffractometer with Ni-filtered $\text{Cu-K}\alpha_1$ radiation (40 kV, 40 mA, 1.5406 Å). XPS measurements were conducted on a PHI 5000 VersaProbe system using an $\text{Mg-K}\alpha$ X-ray source.

Gas sensing performance measurements

For the gas sensing measurements, hierarchical highly ordered nanobowl $\text{SnO}_2@ZnO$ NWs were prepared in situ on MEMS heating appliances. Then, the ultrasonic wire bonding technique was applied to connect the fabricated MEMS device with the external circuit. A JF02F gas sensing measurement system was used to characterize the sensing characteristics of the fabricated hierarchical highly ordered nanobowl $\text{SnO}_2@ZnO$ NW sensors for reducing gases, namely, H_2S , NH_3 , CH_3COCH_3 , C_7H_8 , and HCHO . In this work, for *n*-type SMO materials, the gas sensing response (*R*) in the reducing-gas measurements was defined as $R = R_a/R_g$, where R_a represents the resistance of materials in air and R_g represents the

resistance in the detecting gas. The response and recovery times were determined as the time required from 10 to 90% of the highest response variation when exposed to the target gas and air, respectively. The measurements under different temperatures were conducted to investigate the optimal operating temperature for our sensors. Moreover, to determine the long-term stability and repeatability, the H₂S sensing performance of the hierarchical highly ordered nanobowl SnO₂@ZnO NW sensor preserved in an air atmosphere was characterized again after a month.

Conclusions

In conclusion, hierarchical highly ordered SnO₂ nanobowl branched ZnO NWs were synthesized through a sequential process combining hard template processing, atomic-layer deposition and hydrothermal processing. The designed hierarchical sensing materials were prepared in situ on MEMS, which is expected to achieve long-term stability and low power consumption. Specifically, the hierarchical nanobowl SnO₂@ZnO NW sensor displayed a high sensitivity (R_a/R_b) of 6.24, a fast response and recovery speed (i.e., 14 s and 39 s, respectively), and an excellent selectivity when detecting 1 ppm H₂S at 250 °C, whose rate of resistance change (i.e., 5.24) is 2.6 times higher than that of the pristine SnO₂ nanobowl sensor. The substantially improved sensing performance could be mainly attributed to the synergistic effect of the hierarchical heterostructures, including increased specific surface area, the formation of heterojunctions and homojunctions, as well as the additional reaction between ZnO and H₂S. Based on our results, such well-designed hierarchical highly ordered nanobowl SnO₂@ZnO NW gas sensors are good candidates for enhanced sensitive and selective H₂S detection with long-term stability and repeatability.

Acknowledgements

This work was supported by the National Natural Science Foundation of China (No. U1632121, 51861135105, and 61874034), Basic Research Project of Shanghai Science and Technology Innovation Action (No. 17JC1400300), Natural Science Foundation of Shanghai (No. 18ZR1405000), and China Postdoctoral Science Foundation (No. TQ20190067).

Author contributions

LY.Z., K.P.Y., and H.L.L. conceived and designed the project. LY.Z. and K.P.Y. performed the experiments. LY.Z., K.P.Y., J.H.Y., C.Z.H., H.P.M., X.M.J., A.D., H.L.L., and D.W.Z. analyzed the data. LY.Z., K.P.Y. and H.L.L. wrote the manuscript. All authors discussed the results and commented on the manuscript.

Conflict of interest

The authors declare that they have no conflict of interest.

Supplementary information accompanies this paper at <https://doi.org/10.1038/s41378-020-0142-6>.

Received: 12 November 2019 Revised: 25 December 2019 Accepted: 2 January 2020

Published online: 04 May 2020

References

- Chen, Y., Xu, P., Xu, T., Zheng, D. & Li, X. ZnO-nanowire size effect induced ultra-high sensing response to ppb-level H₂S. *Sens. Actuators B* **240**, 264–272 (2017).
- Kaur, M. et al. Room-temperature H₂S gas sensing at ppb level by single crystal In₂O₃ whiskers. *Sens. Actuators B* **133**, 456–461 (2008).
- Wang, Y. et al. Low-temperature H₂S sensors based on Ag-doped α-Fe₂O₃ nanoparticles. *Sens. Actuators B* **131**, 183–189 (2008).
- Guo, W., Mei, L., Wen, J. & Ma, J. High-response H₂S sensor based on ZnO/SnO₂ heterogeneous nanospheres. *RSC Adv.* **6**, 15048–15053 (2016).
- Sukunta, J., Wisitsoraat, A., Tuantranont, A., Phanichphant, S. & Liewhiran, C. Highly-sensitive H₂S sensors based on flame-made V-substituted SnO₂ sensing films. *Sens. Actuators B* **242**, 1095–1107 (2017).
- Liang, X. et al. Solid-state potentiometric H₂S sensor combining NASICON with Pr₆O₁₁-doped SnO₂ electrode. *Sens. Actuators B* **125**, 544–549 (2007).
- Varga, A., Bozóki, Z., Szakáll, M. & Szabó, G. Photoacoustic system for on-line process monitoring of hydrogen sulfide (H₂S) concentration in natural gas streams. *Appl. Phys. B* **85**, 315–321 (2006).
- Ma, J. et al. Pt nanoparticles sensitized ordered mesoporous WO₃ semiconductor: gas sensing performance and mechanism study. *Adv. Funct. Mater.* **28**, 1705268 (2018).
- Wang, Y. et al. Fabrication and gas sensing properties of Au-loaded SnO₂ composite nanoparticles for highly sensitive hydrogen detection. *Sens. Actuators B* **240**, 664–673 (2017).
- Choi, K. S., Park, S. & Chang, S.-P. Enhanced ethanol sensing properties based on SnO₂ nanowires coated with Fe₂O₃ nanoparticles. *Sens. Actuators B* **238**, 871–879 (2017).
- Zou, Y. et al. Highly efficient gas sensor using a hollow SnO₂ microfiber for triethylamine detection. *ACS Sens.* **2**, 897–902 (2017).
- Jeon, J.-M. et al. Vertically ordered SnO₂ nanobamboos for substantially improved detection of volatile reducing gases. *J. Mater. Chem. A* **3**, 17939–17945 (2015).
- Bulemo, P. M., Cho, H. J., Kim, D. H. & Kim, I. D. Facile synthesis of Pt-functionalized meso/macroporous SnO₂ hollow spheres through in situ templating with SiO₂ for H₂S sensors. *ACS Appl. Mater. Interfaces* **10**, 18183–18191 (2018).
- Ni, Y. et al. High response to nitrogen dioxide derived from antimony peroxide modified tin oxide porous nanocomposites serving as gas sensing material. *Sens. Actuators B* **247**, 216–223 (2017).
- Xu, L. et al. Micro/Nano gas sensors: a new strategy towards in-situ wafer-level fabrication of high-performance gas sensing chips. *Sci. Rep.* **5**, 10507 (2015).
- Dai, Z., Lee, C.-S., Tian, Y., Kim, I.-D. & Lee, J.-H. Highly reversible switching from P- to N-type NO₂ sensing in a monolayer Fe₂O₃ inverse opal film and the associated P-N transition phase diagram. *J. Mater. Chem. A* **3**, 3372–3381 (2015).
- Ge, W. et al. In₂O₃-SnO₂ hybrid porous nanostructures delivering enhanced formaldehyde sensing performance. *J. Alloy. Compd.* **746**, 36–44 (2018).
- Gu, F., Wang, H., Han, D. & Wang, Z. Enhancing the sensing performance of SnO₂ inverse opal thin films by In and Au doping. *Sens. Actuators B* **245**, 1023–1031 (2017).
- Xiao, L., Xu, S., Yu, G. & Liu, S. Efficient hierarchical mixed Pd/SnO₂ porous architecture deposited microheater for low power ethanol gas sensor. *Sens. Actuators B* **255**, 2002–2010 (2018).
- Yang, D.-J., Kamiencick, I., Youn, D. Y., Rothschild, A. & Kim, I.-D. Ultrasensitive and highly selective gas sensors based on electrospun SnO₂ nanofibers modified by Pd loading. *Adv. Funct. Mater.* **20**, 4258–4262 (2010).
- Li, Y. X. et al. Hierarchical morphology-dependent gas-sensing performances of three-dimensional SnO₂ nanostructures. *ACS Sens.* **2**, 102–110 (2017).
- Gu, D., Li, X., Zhao, Y. & Wang, J. Enhanced NO₂ sensing of SnO₂/SnS₂ heterojunction based sensor. *Sens. Actuators B* **244**, 67–76 (2017).
- Tomer, V. K. & Duhan, S. Ordered mesoporous Ag-doped TiO₂/SnO₂ nanocomposite based highly sensitive and selective VOC sensors. *J. Mater. Chem. A* **4**, 1033–1043 (2016).
- Alenezi, M. R., Henley, S. J., Emerson, N. G. & Silva, S. R. From 1D and 2D ZnO nanostructures to 3D hierarchical structures with enhanced gas sensing properties. *Nanoscale* **6**, 235–247 (2014).
- Zhang, Z. et al. Novel SnO₂@ZnO hierarchical nanostructures for highly sensitive and selective NO₂ gas sensing. *Sens. Actuators B* **257**, 714–727 (2018).
- Zhu, L.-Y. et al. Enhanced piezoelectric performance of the ZnO/AlN stacked nanofilm nanogenerator grown by atomic layer deposition. *APL Mater.* **6**, 121109 (2018).

27. Guo, W. et al. Gas-sensing performance enhancement in ZnO nanostructures by hierarchical morphology. *Sens. Actuators B* **166-167**, 492–499 (2012).
28. Pérez-González, M., Tomás, S. A., Santoyo-Salazar, J. & Morales-Luna, M. Enhanced photocatalytic activity of TiO₂-ZnO thin films deposited by dc reactive magnetron sputtering. *Ceram. Int.* **43**, 8831–8838 (2017).
29. Wang, L. et al. Construction of 1D SnO₂-coated ZnO nanowire heterojunction for their improved n-butylamine sensing performances. *Sci. Rep.* **6**, 35079 (2016).
30. Zhu, L.-Y. et al. Fabrication of heterostructured p-CuO/n-SnO₂ core-shell nanowires for enhanced sensitive and selective formaldehyde detection. *Sens. Actuators B* **290**, 233–241 (2019).
31. Huang, J. et al. Large-scale selective preparation of porous SnO₂ 3D architectures and their gas-sensing property. *CrystEngComm* **14**, 3283–3290 (2012).
32. Fan, X. X., Xu, Y. J., He, W. M., Huang, X. & He, X. L. UV-enhanced NO₂ gas sensor based on electrospinning SnO₂-ZnO composite nanofibers. *IOP Conf. Ser. Mater. Sci. Eng.* **479**, 012121 (2019).
33. Khoang, N. D., Trung, D. D., Van Duy, N., Hoa, N. D. & Van Hieu, N. Design of SnO₂/ZnO hierarchical nanostructures for enhanced ethanol gas-sensing performance. *Sens. Actuators B* **174**, 594–601 (2012).
34. Gong, H., Zhao, C. & Wang, F. On-chip growth of SnO₂/ZnO core-shell nanosheet arrays for ethanol detection. *IEEE Electron Device Lett.* **39**, 1065–1068 (2018).
35. Tang, W. & Wang, J. Methanol sensing micro-gas sensors of SnO₂-ZnO nanofibers on Si/SiO₂/Ti/Pt substrate via stepwise-heating electrospinning. *J. Mater. Sci.* **50**, 4209–4220 (2015).
36. Cho, I., Kang, K., Yang, D., Yun, J. & Park, I. Localized liquid-phase synthesis of porous SnO₂ nanotubes on MEMS platform for low-power, high performance gas sensors. *ACS Appl. Mater. Interfaces* **9**, 27111–27119 (2017).
37. Wang, L. et al. 3D porous ZnO-SnS p-n heterojunction for visible light driven photocatalysis. *Phys. Chem. Chem. Phys.* **19**, 16576–16585 (2017).
38. Hosseini, Z. S., zad, A. I. & Mortezaali, A. Room temperature H₂S gas sensor based on rather aligned ZnO nanorods with flower-like structures. *Sens. Actuators B* **207**, 865–871 (2015).
39. Li, S., Lu, Z., Yang, Z. & Chu, X. The sensing mechanism of Pt-doped SnO₂ surface toward CO: a first-principle study. *Sens. Actuators B* **202**, 83–92 (2014).
40. Fu, D., Zhu, C., Zhang, X., Li, C. & Chen, Y. Two-dimensional net-like SnO₂/ZnO heteronanostructures for high-performance H₂S gas sensor. *J. Mater. Chem. A* **4**, 1390–1398 (2016).
41. Liu, Z., Fan, T., Zhang, D., Gong, X. & Xu, J. Hierarchically porous ZnO with high sensitivity and selectivity to H₂S derived from biotemplates. *Sens. Actuators B* **136**, 499–509 (2009).
42. Vuong, N. M., Chinh, N. D., Huy, B. T. & Lee, Y.-I. CuO-decorated ZnO hierarchical nanostructures as efficient and established sensing materials for H₂S gas sensors. *Sci. Rep.* **6**, 26736 (2016).
43. Pan, Z. et al. Electrodeposition-based in situ construction of a ZnO-ordered macroporous film gas sensor with enhanced sensitivity. *J. Mater. Chem. A* **7**, 1287–1299 (2019).
44. Bai, S. et al. Synthesis of SnO₂-CuO heterojunction using electrospinning and application in detecting of CO. *Sens. Actuators B* **226**, 96–103 (2016).
45. Poloju, M., Jayababu, N., Manikandan, E. & Ramana Reddy, M. V. Enhancement of the isopropanol gas sensing performance of SnO₂/ZnO core/shell nanocomposites. *J. Mater. Chem. C* **5**, 2662–2668 (2017).
46. Choi, M. S. et al. Promotional effects of ZnO-branching and Au-functionalization on the surface of SnO₂ nanowires for NO₂ sensing. *J. Alloy. Compd.* **786**, 27–39 (2019).
47. Yuan, K. et al. Synthesis of WO₃@ZnWO₄@ZnO-ZnO hierarchical nanocactus arrays for efficient photoelectrochemical water splitting. *Nano Energy* **41**, 543–551 (2017).
48. Yan, S. H. et al. Synthesis of SnO₂-ZnO heterostructured nanofibers for enhanced ethanol gas-sensing performance. *Sens. Actuators B* **221**, 88–95 (2015).
49. Kim, J. & Yong, K. Mechanism study of ZnO nanorod-bundle sensors for H₂S gas sensing. *J. Phys. Chem. C* **115**, 7218–7224 (2011).
50. Yuan, K. et al. Designed fabrication and characterization of three-dimensionally ordered arrays of core-shell magnetic mesoporous carbon microspheres. *ACS Appl. Mater. Interfaces* **7**, 5312–5319 (2015).
51. Zhang, Y. et al. Photoluminescence enhancement of ZnO nanowire arrays by atomic layer deposition of ZrO₂ layers and thermal annealing. *Phys. Chem. Chem. Phys.* **18**, 16377–16385 (2016).